


Machine-Learning-Assisted Acoustic Consecutive Fano Resonances: Application to a Tunable Broadband Low-Frequency Metasilencer

Zi-xiang Xu,^{1,2} Bin Zheng,^{1,2} Jing Yang^{1,2,*}, Bin Liang,^{1,2} and Jian-chun Cheng^{1,2}

¹Key Laboratory of Modern Acoustics, MOE, Institute of Acoustics, Department of Physics, Nanjing University, Nanjing 210093, People's Republic of China

²Collaborative Innovation Center of Advanced Microstructures, Nanjing University, Nanjing 210093, People's Republic of China

 (Received 11 July 2021; revised 16 September 2021; accepted 22 September 2021; published 13 October 2021)

The Fano resonance is a widespread wave-scattering phenomenon associated with an ultrasharp line shape, which just serves a narrow working frequency range around the interference frequency, rendering the realization of Fano-based applications extremely challenging. Here, we present and experimentally verify a mechanism of acoustic consecutive Fano resonances (ACFRs) with a symmetric profile for broadband sound attenuation, and extend to a practical implementation of a tunable low-frequency double-helix metasilencer. Based on the ACFRs' dependence on material parameters in the bilayer metamaterial model, we employ an inverse design using Bayesian machine learning to search the optimal broadband insulating performance with a rapid convergence speed (15 iterations). For practical requirement, we extend the ACFRs' prototype to a continuously tunable double-helix metastructure for broadband low-frequency sound attenuation. This broadband effect can be interpreted by the dual-band single-negativity property. A good agreement between numerical simulation and experiment evidences the effectiveness of the proposed metasilencer with tunable sound attenuation (>90%) in 425–865 Hz and high ventilation (>80%) at various double-helix combinations. Our proposed ACFRs' mechanism and its associated metastructure would open routes to promising acoustic metamaterial-based applications, such as filtering, switching, and sensing, and beyond.

DOI: [10.1103/PhysRevApplied.16.044020](https://doi.org/10.1103/PhysRevApplied.16.044020)

I. INTRODUCTION

In recent decades, the Fano resonance [1,2] has become a research hotspot because of its applications in various branches of science and engineering like atomic and solid-state physics [3,4], electromagnetism [5], electronic circuits [6], photonics [7,8], nonlinear optics [9], and acoustics [10,11]. Fano resonance with asymmetric profile and ultranarrow linewidth is induced by the interference between a discrete resonant state and a smooth continuum state in background media, which limits its application in many actual wideband scenarios with complex frequency components. It is desired to break the narrow-bandwidth limitation of Fano resonance in physics, and consequently to obtain a broad working frequency range. With the advances of optical metamaterials, the constructive idea of consecutive Fano resonances [12–14] (CFRs) was introduced to extend the operation bandwidth. Wu *et al.* proposed a concept of a low-symmetry three-dimensional metamaterial to exhibit optical CFRs, slowing down light over a spectrally broad band [13]. CFRs of high-contrast

dielectric gratings were used to design broadband filters whose lineshapes have mirror symmetry [14]. However, acoustic consecutive Fano resonances (ACFRs) have not been mentioned until now, which may have potential in some real acoustic applications, such as acoustic filters, switches, and sensors, etc.

Conventional acoustic metamaterial (AM) design has relied on extensive experimentation and a trial-and-error approach where analytical or computational models provide only *a posteriori* explanations. With advances in computational engineering, inverse design of AMs for desired material properties has been performed using intelligent algorithms [15–22], including genetic algorithm (GA) [15,16], and artificial neural network (ANN) [18–21], etc. However, a major drawback of GA is slow convergence speed because the fit individuals quickly degenerate in mutation. Machine learning using ANN may require large amounts of data for training and could often be notoriously difficult to train. Recently, machine learning using the Gauss-Bayesian (GB) model has emerged as a low-cost and flexible solution for AM inverse design [22]. The GB model provides an adaptive paradigm to sample the design space more efficiently for identifying the global

*yangj@nju.edu.cn

optimum by properly selecting the Gaussian kernel and acquisition function without large database. In addition, the direct mapping relationships between metamaterial input parameters and particular functionalities enables the parameters to be inversely adjusted independently from physical models.

As a problem in acoustics, low-frequency (<1000 Hz) sound insulation finds wide applications in diverse application scenarios. In recent years, researchers have put forward a few AM proposals addressing the challenge of sound attenuation [23–32]. Zhang *et al.* proposed a narrowband Fano-based low-frequency sound silencer, while comprising a large open area for air passage [31]. Furthermore, a strategy for broadband shielding is theoretically proposed with a helical metasurface [32]. However, the aforementioned existing AMs with predefined microstructures can operate only in a fixed frequency range [33]. To break this restriction, increased attention has been paid to AMs with reconfigurable metastructure [34–38]. Typically, coding metamaterials [36] and programming metamaterials [37] have demonstrated numerous intriguing properties, such as anomalous reflection and refraction [39,40], wave bending [41,42], and wave focusing [43], etc. Both of them were based on the assembly of various fixed components, and therefore, are inflexible and not continuously adjustable. Hence, a continuously tunable self-assembling structure would be tremendously helpful to realize the flexible acoustic metamaterials and expand the working bandwidth.

In this work, we propose and experimentally demonstrate a mechanism of symmetric profile ACFRs for broadband sound suppression and present a practical application of a tunable low-frequency double-helix metasilencer. To remove the narrowband restriction of Fano resonance, we employ an inverse method based on machine learning using the GB model to seek the material parameters in the bilayer metamaterial to obtain the optimal ACFRs' insulating spectrum. Considering the key problem of broadband low-frequency sound attenuation, we

extend the above ACFRs' prototype to a tunable double-helix metasilencer and interpret its broadband effect by the dual-band single-negativity property. Continuously tunable resonance spectral shift of ACFRs can be realized via rotating this self-assembling double-helix metastructure. An agreement between numerical and experimental results validates the effectiveness of the proposed metasilencer, bearing the advantages of broadband low-frequency sound attenuation, continuous tunability, and high ventilation performance.

II. MACHINE-LEARNING-ASSISTED ACFRS IN THE BILAYER METAMATERIAL

Previous studies introduced the acoustic Fano resonance with narrowband characteristic as a result of the interference between the discrete resonant and continuum states [11,31]. Here, we present a mechanism of ACFRs because of the consecutive interferences between the above two states in the bilayer metamaterial. According to the effective-medium theory [44], region 1 ($r < r_1$) is composed of a material with acoustic refractive index of n_1 and mass density of ρ_1 , and region 2 ($r_1 < r < r_2$) is composed of a material with acoustic refractive index of n_2 and mass density of ρ_2 [Fig. 1(a)]. Two regions are separated with the acoustically rigid spacer at ($r = r_1$) of negligible thickness that eliminates the cross-coupling between them. The entire metamaterial is assumed to be confined within a rigid circular waveguide filled with a medium with acoustic refractive index of n_1 and mass density of ρ_1 for the purposes of obtaining the acoustic transmission spectrum. Imagine that an incident acoustic wave along z direction in a waveguide normally impinges the bilayer metamaterial. Then ACFRs of symmetric transmission profile occur due to the fact that the portion of the acoustic wave traveling through region 2 interferes consecutively with the portion of the acoustic wave traveling through region 1. As shown in Fig. 1(b), region 1 remaining in a continuum state always allows a high transmission.

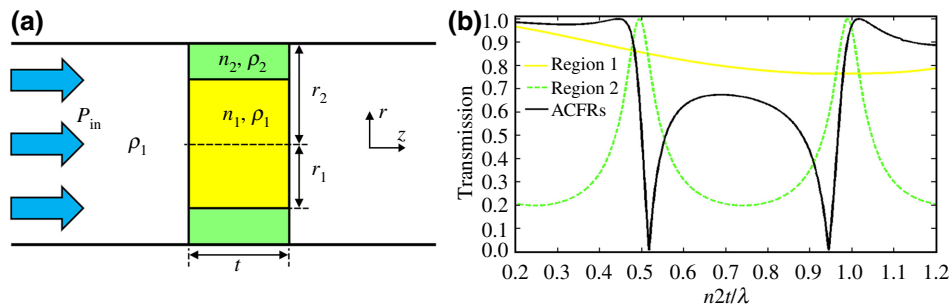


FIG. 1. (a) Schematic diagram of the bilayer metamaterial placed perpendicular to the direction of wave propagation. The two-colored parts of the metamaterial are characterized by two effective mediums with different acoustic properties. (b) Transmission spectra through region 1, region 2, and the bilayer metamaterial, respectively. Here, the radius ratio $r_1/r_2=0.5$, the refractive index ratio $n_1/n_2=0.2$, and mass density ratio $\rho_1/\rho_2=0.1$.

Region 2, which provides the resonant state, possesses two consecutive transmission peaks where the Fabry-Perot resonances occur. The N th order Fabry-Perot resonance occurs at $n_2 t = N\lambda/2$. Here, $N = 1$ and 2 are used in this work. The transmission of the whole bilayer metamaterial illustrates that the transmission peaks of ACFRs occur outside these Fabry-Perot resonances, the transmission dips take place inside, and the areas are bounded by the specular Fabry-Perot resonances. Of note, the polarity of the Fano resonance, i.e., the relative spectral position of the

peak and the dip in the Fano resonance spectrum [45] flips when a Fabry-Perot resonance is passed, which shapes two asymmetric Fano profiles into a symmetric ACFR profile. This symmetry is critical for the formation of the middle broadband transmission region between two Fano resonance dips, as it enables the resonance spectra of two Fano resonances to merge without passing through a zero.

We first perform comparative simulations to study the relationship between material parameters and the occurrence of broad low-transmission band of ACFRs. As

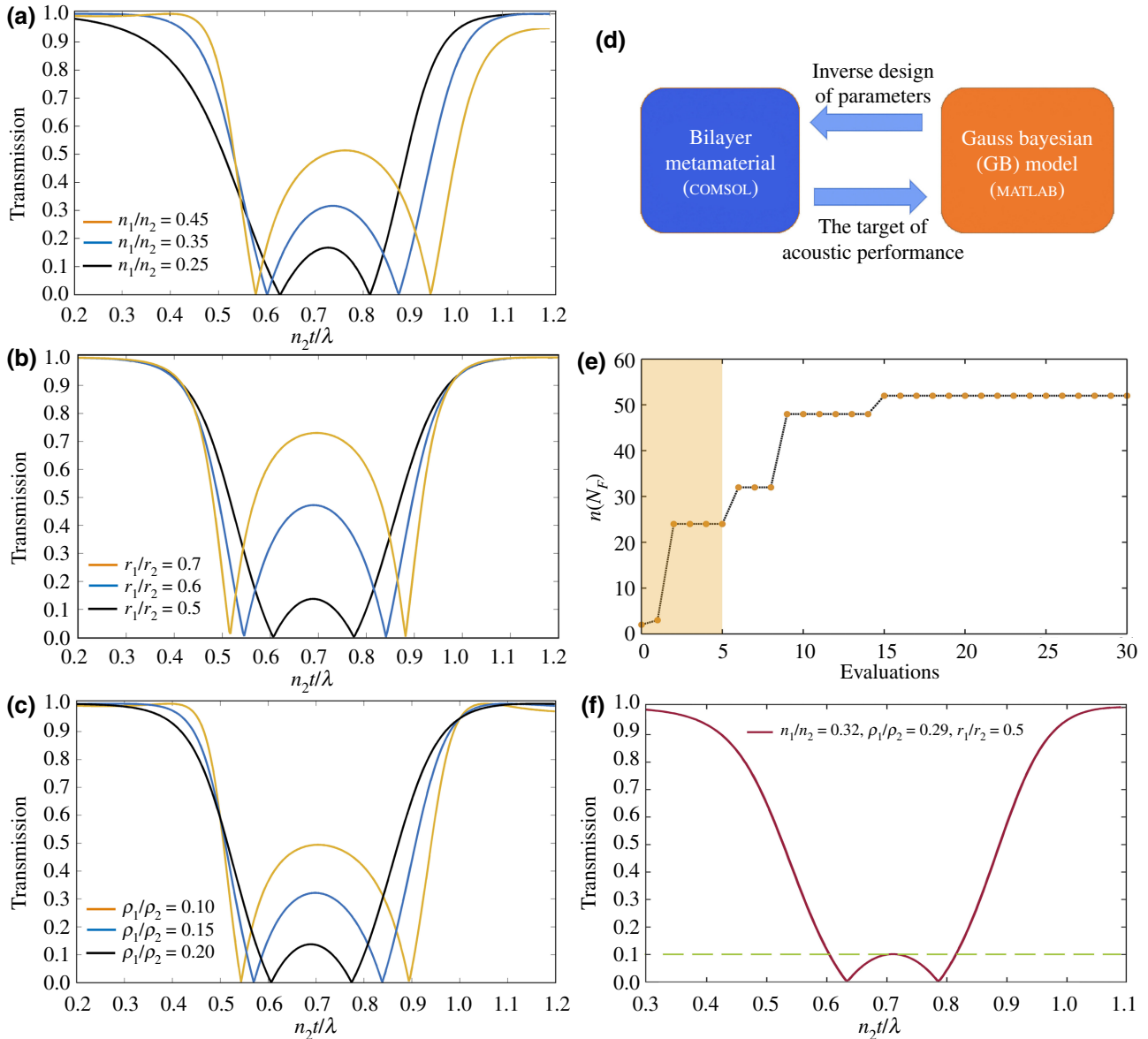


FIG. 2. (a) Transmission spectra through the bilayer metamaterial for various values n_1/n_2 ($r_1/r_2 = 0.5$ and $\rho_1/\rho_2 = 0.2$). (b) Transmission spectra for different values r_1/r_2 ($n_1/n_2 = 0.25$ and $\rho_1/\rho_2 = 0.2$). (c) Transmission spectra for different values r_1/r_2 ($n_1/n_2 = 0.25$ and $r_1/r_2 = 0.5$). (d) Schematic diagram of the proposed design method. (e) Maximum bandwidth in the current dataset as a function of the number of evaluations, where N_F is the sampling step length in the target frequency range $[0.2n_2t/\lambda, 1.2n_2t/\lambda]$. The initial dataset is marked with brown. (f) The optimal transmission spectrum for the bilayer metamaterial where $n_1/n_2 = 0.32$, $\rho_1/\rho_2 = 0.29$, and $r_1/r_2 = 0.50$.

shown in Figs. 2(a)–2(c), the transmission of the middle region between two Fano resonance dips rises with an increasing value of n_1/n_2 , growing value of r_1/r_2 , and decreasing value of ρ_1/ρ_2 . Of note, there is a trade-off between the transmission and bandwidth of the middle region between two Fano resonance dips. It is difficult to find the optimal parameters and acoustic performance using the forward design method for such multivariate physics problems because it consumes a lot of computing resources simultaneously. Then, we adopt machine learning using the GB model to inversely design the desired ACFRs with maximum low-transmission bandwidth. An optimization framework is set forth with a MATLAB implementation of the GB model used in conjunction with the bilayer metamaterial implemented in the COMSOL Multiphysics pressure acoustic module [46], as shown in Fig. 2(d). The objective function is chosen as the total bandwidth and defined as $F = \sum_{i=1}^n N_F$, where N_F is the sampling step length and n represents the number of N_F where transmission coefficients of the sampling frequency are less than or equal 0.1. In Gaussian process, a Gaussian kernel [47,48] $k(x_j, x_k) = \sigma_{F,m}^2 \exp(-\sqrt{5}r) \left[1 + \sqrt{5}r + (5/3)r^2 \right]$ is selected to fit the function in the current task, where x_j and x_k are the inputs, $r = \sqrt{(x_j - x_k)^T \Lambda_m (x_j - x_k)}$ represents the distance of x_j and x_k in function space, Λ_m is a diagonal matrix of d squared length scales $l_{1:d,m}^2$ in the m th iteration. Here, $\sigma_{F,m}^2$ and $l_{1:d,m}$ are the hyperparameters of the GP as well as the intrinsic parameters of the GB model. The training of the GB model is essential to find an estimate of hyperparameters under which the existing samples have the greatest probability of occurrence. Based on Bayesian inference, the logarithm of the probability (marginal-likelihood function) is calculated as

$$\begin{aligned} \log p(F|x_{1:m}, \alpha_m) &= -\frac{1}{2} F^T K^{-1} F - \frac{1}{2} \log(|K|) \\ &\quad - \frac{m}{2} \log(2\pi), \end{aligned} \quad (1)$$

where $F = [F_1, F_2, \dots, F_m]^T$, $K_{jk} = k(x_j, x_k)$, and m denote output vector, Gaussian kernel matrix and the number of the current data, respectively. The acquisition function reconciles the trade-off between exploration of the search space and exploitation of the current promising areas in the optimization process. Here, UP-confidence-bound (UCB) function is picked up as the acquisition functions, which is defined as

$$F_{\text{UCB}m}(x) = \mu_m(x) + \beta \sigma_m(x), \quad (2)$$

where μ_m , σ_m , and β are the posterior mean, uncertainty, and the trade-off index, respectively. To accelerate convergence, adaptive acquisition function is creatively

employed in the GB model by adjusting the index β automatically to balance exploitation and exploration. Due to the use of adaptive acquisition functions, GB machine learning allows the parameters of AMs to be highly efficiently designed. To illustrate the convergence rate in the design, Fig. 2(e) shows the maximum bandwidth in the current dataset plotted as a function of the number of iterations. The current maximum rises steadily just through 15 evaluations, including the establishment of the five initial dataset and ten iterations. It can be seen that the maximum bandwidth expanded by 126% from the initial $23N_F$ to the final $52N_F$. Such GB machine learning assists the bilayer metamaterial to produce a broadband and low-transmission ACFR spectrum, breaking the narrowband physics limitation of Fano resonance. To illustrate the broadband sound suppression of ACFRs, Fig. 2(f) shows the optimal transmission spectrum for the bilayer metamaterial as a function of $n_2 t/\lambda$, where the refractive index ratio (n_1/n_2), mass density ratio (ρ_1/ρ_2), and radius ratio (r_1/r_2) are 0.32, 0.29, and 0.50, respectively. The rationale for this machine-learning-assisted broadband effect is the strength of ACFRs is enhanced, i.e., more interference coupling occurs between the resonant scattering of a discrete state and the background scattering of a continuous state. As the coupling increases, consecutive Fano resonances broaden to the extent that they overlap, forming broad regions of uniformly high reflection.

III. ACFR REALIZATION: TUNABLE LOW-FREQUENCY DOUBLE-HELIX METASILENCER

A. Double-helix metastructure with continuous tunability

In order to achieve continuously tunable characteristics, we propose a double-helix metastructure consisting of a set of matched internal and external helices based on the bilayer metamaterial, as shown in Fig. 3(a). The matched double helices contain hollow and helical channels, corresponding to region 1 and 2 of the bilayer metamaterial, respectively. The central channel of the metastructure ($r < r_1$) is a completely open area, which yields nature air transport, whose refractive index $n_1 = 1$. In the helical channel ($r_1 < r < r_3$), four air passages are coiled by double helix in which the extended path length of the acoustic wave provides a large effective refractive index n_2 [49]. The four air channels can still ensure a high degree of air circulation. The difference in acoustic properties of the two channels may provide the discrete resonant state in the helical channel, whereas the central channel remains in the continuum state. Note that the internal helix can be screwed flexibly into the external helix, thus realizing continuously tunable channel length, without changing the original structure. It is such a continuous tunability that

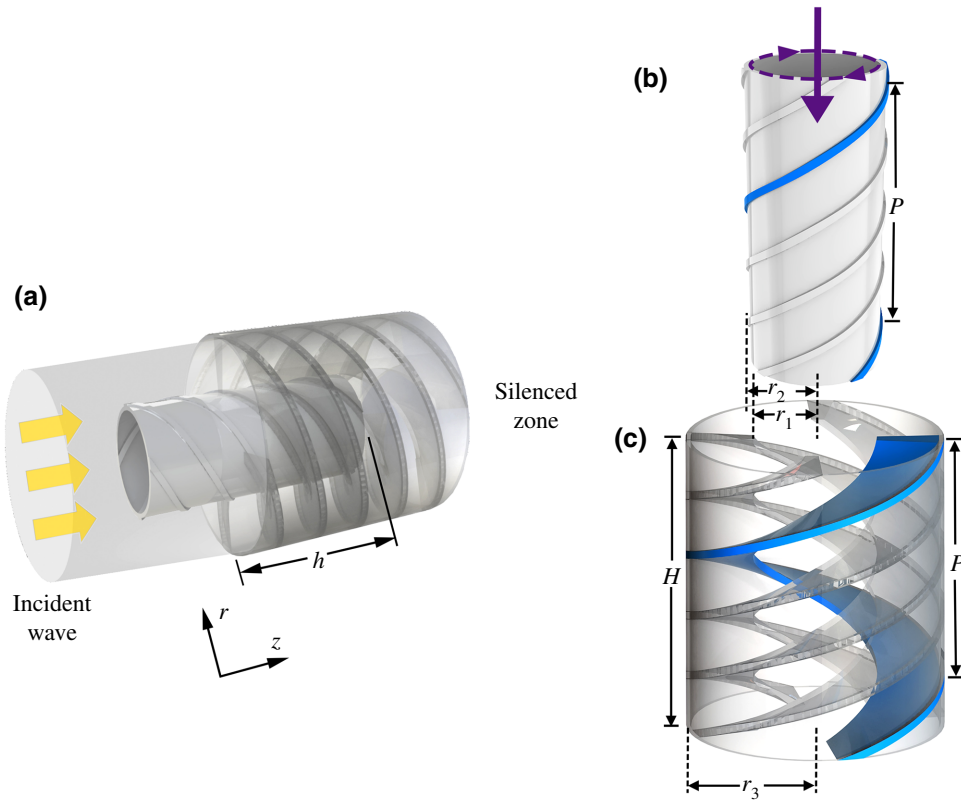


FIG. 3. (a) Schematic diagram of the double-helix metasilencer placed perpendicular to the direction of wave propagation. The internal helix can be continuously screwed into the external helix. (b), (c) Geometrical details of the internal and external helices.

makes a single structure for different working frequencies possible. The proposed metastructure involves inner radius r_1 , outer radius of internal helix with thread r_2 , outer radius r_3 , helical depth h , and the total thickness H . Figures 3(b) and 3(c) illustrate the matched internal and external helices, whose spatial constructs can be described by Eqs. (3) and (4), respectively, as

$$\begin{cases} x = r \sin(\theta + \varphi), \\ y = r \cos(\theta + \varphi), & \theta \in [0, \theta_0], r \in [r_1, r_2], \\ z = P\theta/(2\pi), \end{cases} \quad (3)$$

$$\begin{cases} x = r \sin(\theta), \\ y = r \cos(\theta), & \theta \in [0, \theta_0], r \in [r_1, r_3], \\ z = P\theta/(2\pi), \end{cases} \quad (4)$$

where r and θ represent the radius and angle of the blades, respectively; P expresses the parameter to describe the variable spacing of helical pitch.

B. ACFR performance and effective properties of the metasilencer

Inspired by the ACFRs' prototype in the bilayer metamaterial, we design a tunable broadband low-frequency metasilencer using the double-helix metastructure, providing rich geometrical parameters to flexibly tune its acoustic property. The coupling of the discrete resonant and continuum states of ACFRs are affected by the various inner

radius r_1 and variable spacing of helical pitch P . The former corresponds to the radius ratio in the bilayer metamaterial. The latter is related to the refractive index and mass density ratios. Based on the GB-based machine-learning method, one could find the optimal values to achieve a broadband spectrum with low transmission. Here, the detailed geometrical parameters are presented in Table I. The corresponding relative refractive index and relative mass density ratios in the double-helix metastructure is provided within the Supplemental Material [46].

Under the above geometrical parameters, the thickness of our metasilencer is only 0.03λ of the lowest working frequency. As shown in Fig. 4(a), the central channel provides the continuum state. While the helical channel, remaining in the discrete resonant state, behaves as a linear resonator, possessing two consecutive Fabry-Perot resonances at 340 and 685 Hz, respectively. The N th order Fabry-Perot resonance of the helical channel occurs at $n_2 h = N c_0 / 2f$, where c_0 is the velocity in air. The weak coupling between these two states induces resonance and antiresonance at 320 and 430 Hz and at 695

TABLE I. Geometrical parameters of the double-helix metasilencer.

r_1 (mm)	r_2 (mm)	r_3 (mm)	θ_0 (rad)	P (mm)	H (mm)	φ (rad)
25.0	26.0	50.0	14.2	66.3	150.0	0.21

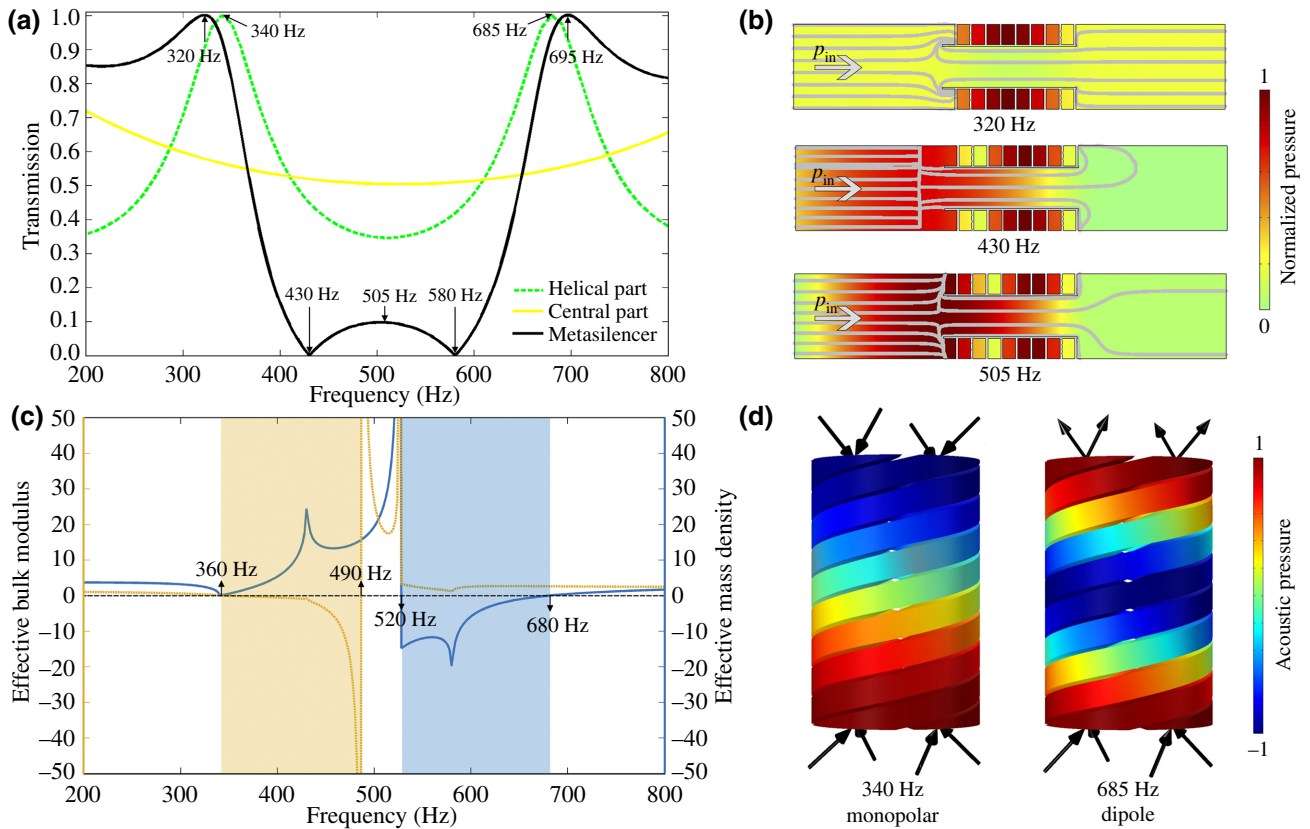


FIG. 4. (a) Transmission spectra of the helical channel, central channel, and the whole metasilencer ($h = 150$ mm). (b) Sound-pressure distributions and velocity streamlines on a metasilencer cut plane. (c) Illustration for the formation of the negative effective material parameters. The negative EBM and EMD frequency ranges are shaded orange and blue, respectively, and the positive passband is white. (d) Sound-pressure distributions and local velocity at two surfaces of the helical channel at the monopole and dipole modes.

and 580 Hz, respectively. It is noteworthy that the distributions of the resonances and antiresonances are in the opposite order. Hence, this ACFR-based metasilencer can block more than 90% incident sound waves in the range of 409–605 Hz ($h = 150$ mm). Considering the symmetric profile of ACFRs, three representative frequencies (320, 430, and 505 Hz) corresponding to transmission peak, dip, and middle region, respectively, are chosen to visualize the insulating performance of the metasilencer [Fig. 4(b)]. Complete transmission peak can be observed in the output side of the metasilencer, indicating the induced resonance mode. Zero transmission dip occurs at the antiresonance point, revealing the interference pattern in the output side between the continuum state of central channel and discrete resonant state of the helical channel. A remarkably degraded amplitude and localized streamline at 505 Hz indicates that sound blocking is consistently effective in the whole middle frequency range in between. Beyond that, the proposed metasilencer is effective under a wide-angle range of incidence, which is given within the Supplemental Material [46].

Furthermore, to gain a deeper insight into the physical mechanism of the designed broadband metasilencer, we

propose a physical model based on effective mass density (EMD) and effective bulk modulus (EBM) retrieved from the reflection and transmission coefficients [50]. In Fig. 4(c), a dual-band single-negativity band, i.e., a negative EBM (360–490 Hz) and a negative EMD (520–680 Hz) are obtained, which coincide with the broad sound insulation band. Single negativity in the effective parameters gives rise to a pronounced imaginary part of the effective wave vectors within the band gaps even in the absence of dissipative effects, so that the acoustic wave must be evanescent [51]. Therefore, the broadband sound attenuation can be achieved in this dual-band single-negativity case. Additionally, the monopolar mode and dipolar mode are illustrated in Fig. 4(d), where arrows represent the local velocity at two surfaces of the helical channel. It is noteworthy that the negative bulk modulus is responsible for the first Fano resonance with the monopolar mode and the negative density can be used to capture the second Fano resonance with the dipolar mode. The monopolar mode at 340 Hz and dipolar one at 685 Hz excited the mentioned two sets of resonance and antiresonance modes to generate a broadband low-transmission spectrum.

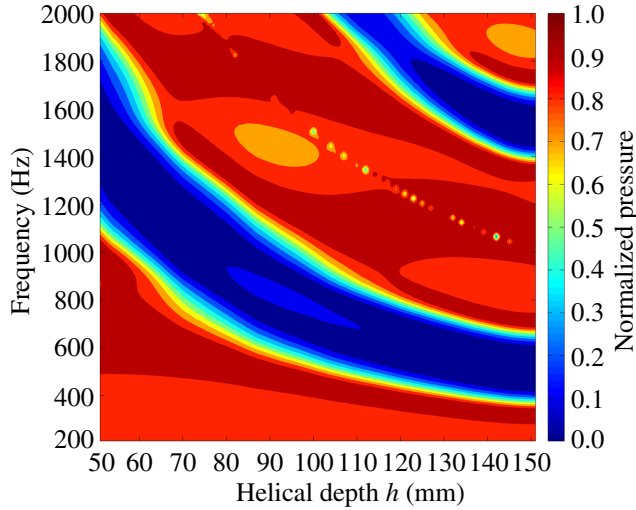


FIG. 5. Transmission spectra of the tunable double-helix metasilencer versus the helical depth h .

C. Continuously tunable ACFR spectra

Thanks to continuous tunability of the proposed double-helix metastructure, selective ACFRs insulating bands of the metasilencer can be realized by means of screwing the matched internal helix into the external helix. The tuning of double helices leads to the helical depth h altering, accordingly causing the the channel's length, which determines the Fabry-Perot resonances of the helical channel. Here, the specular Fabry-Perot resonances are located at $f = c_0/2n_2h$ and $f = c_0/n_2h$. As mentioned above, the transmission peaks of ACFRs occur outside these Fabry-Perot resonances, the transmission dips take place inside, and the areas are bounded by the Fabry-Perot resonances. Thus, the broadband low-frequency region of ACFRs shifts with Fabry-Perot resonances. Figure 5 illustrates the transmission spectra of the tunable double-helix metasilencer versus helical depth h . The resonance frequencies of ACFRs decrease with the increase of helical depth h , enabling the double-helix metasilencer to possess rich yet selective wide insulation bands. Through tuning the helical depth h (50–150 mm), continuously tunable sound insulation bands from 410 to 1950 Hz can be obtained to further expand the working bandwidth due to the ACFRs' spectrum shift. In addition, it is worth pointing out that the good matching of double helices avoids the acoustic energy leakage in the helical channel of the structure, which is particularly useful for sound insulation device. Therefore, our self-assembling double-helix metastructure is a significant step to promote metamaterials for practical applications.

IV. EXPERIMENTAL DEMONSTRATION

Acoustic attenuation in the low-frequency regime (<1000 Hz) is challenging and necessary. In order to

verify the validity of the tunable metasilencer in the low-frequency regime, experiments are conducted when the chosen helical depth h ranges from 10 to 14 cm. Figures 6(a)–6(c) show the three-dimensionally (3D) printed specimen of the designed double-helix metasilencer, external helix, and internal helix, respectively. The metasilencer sample is made by a printer (type ZRapid iSLA660) with a printing resolution of $100 \mu\text{m}$ and the printing material used here is acrylonitrile butadiene styrene (ABS) plastic, whose density is 1230 kg/m^3 , and in which the speed of sound is 2230 m/s . The internal helix can be tightly screwed in the external helix at various helical depths h . The thicknesses of the cylindrical shell and helical blades are both 2 mm . The raised thread of the internal helix is 1 mm , whose effect on sound waves is negligible. The experiment setup is displayed in Fig. 6(d). The sound transmission loss (STL) of a 3D-printed sample is measured in the impedance tube (Brüel & Kjær type-4206) with a diameter of 10 cm and a plane wave cut-off frequency of approximately 2010 Hz utilizing the two-load method in which open-end and semianechoic terminations are utilized [52]. A sound source (loudspeaker) is mounted at one end of the impedance tube, and a sample is placed in a holder. The loudspeaker generates broadband, stationary random sound waves that propagate as plane waves, ranging from 50 – 1600 Hz . By measuring the sound pressure at four fixed locations (two in the source tube and two in the receiving tube) and calculating the complex transfer function using a four-channel digital frequency analyzer, it is possible to determine the transmission loss of the sample. The microphone used here is a $1/4$ -in. microphone (Brüel & Kjær type-4187). The simulated and experimental results of the transmission loss and transmission as functions of frequency for the tunable metasilencer are illustrated in Figs. 6(e)–6(g). Good agreements can be observed between the simulated and measured results, demonstrating that the propagation of the incident wave is virtually blocked in a wide band except that the simulated transmission is slightly lower than the experimental transmission. The experimental errors are primarily because of the viscous energy dissipation of the sample surfaces and the unavoidable fabrication and assembly errors, which are not taken into consideration in simulations. We discuss the influences of viscothermal loss on insulating performances in detail [46].

For a quantitative estimation of the ventilation property of our metasilencer, we also measure the ventilation rate without and with the metasilencer. An electric fan (type UGREEN LP149) is placed at one end of the impedance tube to generate steady airflow. A wind speed meter (type TECMAN TM856) is placed at another end of the impedance tube and make it parallel to the sample. As shown in Fig. 6(h), the measured ventilation rates at different helical depths (5–14 cm) all exceed 80% , revealing a high-efficiency ventilation performance.

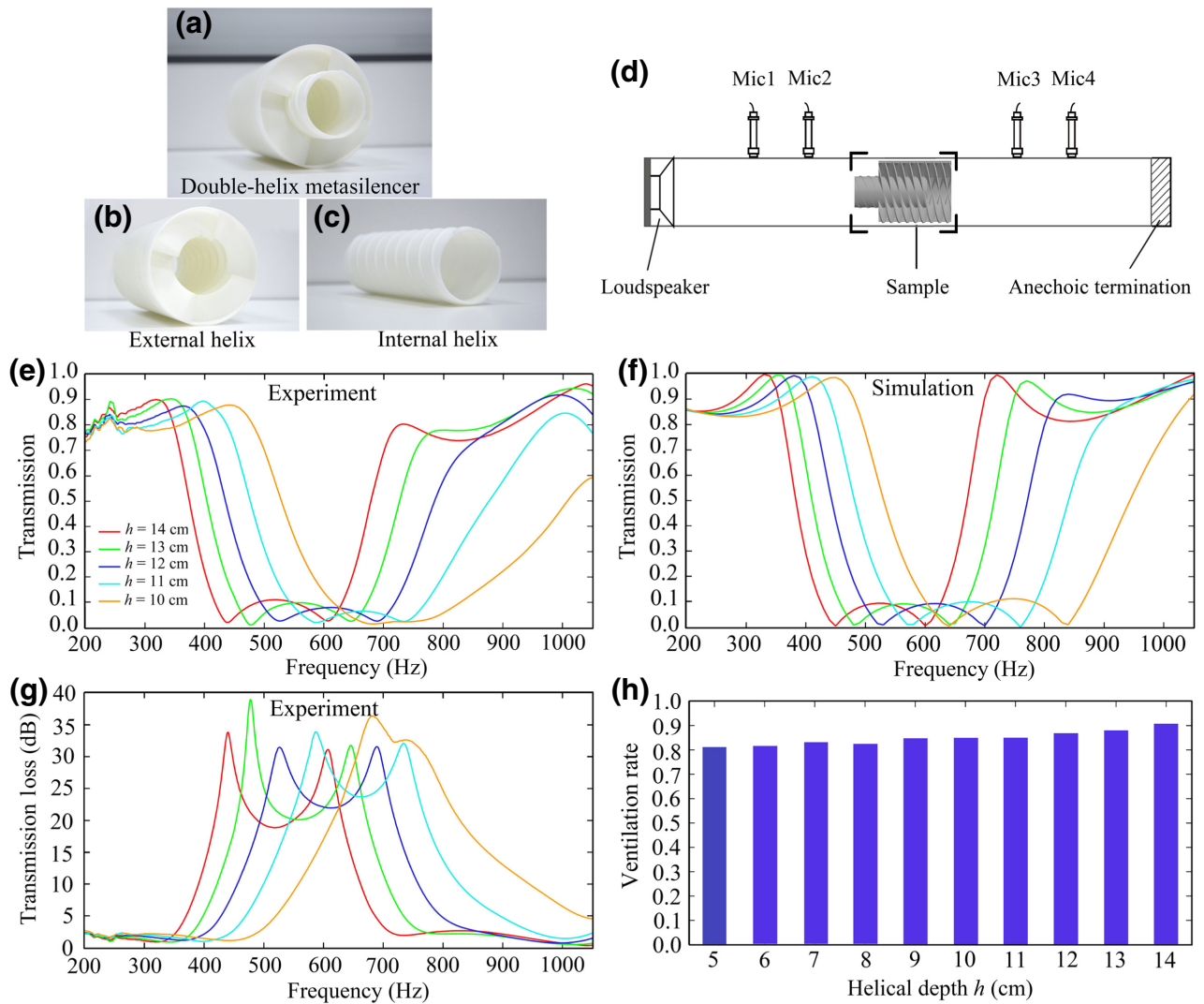


FIG. 6. (a), (b), (c) Photos of the 3D-printed specimen of the designed double-helix metasilencer, external helix, and internal helix, respectively. (d) Schematics of the experimental setup. Measurements of the ventilation rate employ the same experimental setup. (e), (f), (g) Measured transmission loss, measured transmission, and simulated transmission for the metasilencer at various helical depths. (h) Measured ventilation rate for the metasilencer at various helical depths.

V. CONCLUSION

In conclusion, we introduce a mechanism of symmetric profile ACFRs with broadband sound attenuation to break the physic narrowband limitation of conventional Fano resonance. Based on the ACFRs’ dependence of material parameters in the bilayer metamaterial, a fast GB-machine-learning-assisted inverse method is used to obtain the optimal broadband insulating performance. An ACFR practical realization of the double-helix metasilencer is then proposed for continuously tunable broadband low-frequency sound attenuation from 425 to 865 Hz. Consecutive negative EMD and EBM bands derived from ACFRs interpret the generation of broadband sound suppression. Both numerical and experimental results verify the tunable broadband sound attenuation and highly

efficient ventilation capability of the proposed metasilencer. Our proposed ACFR mechanism and its associated metastructure may provide avenues to metamaterial-based applications, such as filtering, switching, and sensing, and beyond.

ACKNOWLEDGMENTS

This work is supported by the National Natural Science Foundation of China (Grants No. 12174190, No. 11634006, and No. 81127901), the Innovation Special Zone of National Defense Science and Technology, High-Performance Computing Center of Collaborative Innovation Center of Advanced Microstructures, and A Project Funded by the Priority Academic Program Development of Jiangsu Higher Education Institutions.

- [1] U. Fano, Effects of configuration interaction on intensities and phase shifts, *Phys. Rev.* **124**, 1866 (1961).
- [2] A. E. Miroshnichenko, S. Flach, and Y. S. Kivshar, Fano resonances in nanoscale structures, *Rev. Modern Phys.* **82**, 2257 (2010).
- [3] O. Újsághy, J. Kroha, L. Szunyogh, and A. Zawadowski, Theory of the Fano Resonance in the STM Tunneling Density of States due to a Single Kondo Impurity, *Phys. Rev. Lett.* **85**, 2557 (2000).
- [4] A. C. Johnson, C. M. Marcus, M. P. Hanson, and A. C. Gosard, Coulomb-Modified Fano Resonance in a One-Lead Quantum Dot, *Phys. Rev. Lett.* **93**, 106803 (2004).
- [5] A. Bärnthaler, S. Rotter, F. Libisch, J. Burgdörfer, S. Gehler, U. Kuhl, and H. J. Stöckmann, Probing Decoherence Through Fano Resonances, *Phys. Rev. Lett.* **105**, 056801 (2010).
- [6] A. Attaran, S. D. Emami, M. R. K. Soltanian, R. Penny, F. Behbahani, S. W. Harun, H. Ahmad, H. A. Abdul-Rashid, and M. Moghavvemi, Circuit model of Fano resonance on tetramers, pentamers, and broken symmetry pentamers, *Plasmonics* **9**, 1303 (2014).
- [7] P. Fan, Z. Yu, S. Fan, and M. L. Brongersma, Optical Fano resonance of an individual semiconductor nanostructure, *Nat. Mater.* **13**, 471 (2014).
- [8] F. Shafiei, F. Monticone, K. Q. Le, X. X. Liu, T. Hartsfield, A. Alù, and X. Li, A subwavelength plasmonic metamolecule exhibiting magnetic-based optical Fano resonance, *Nat. Nanotechnol.* **8**, 95 (2013).
- [9] Y. Wang, L. Liao, T. Hu, S. Luo, L. Wu, J. Wang, Z. Zhang, W. Xie, L. Sun, A. V. Kavokin, X. Shen, and Z. Chen, Exciton-Polariton Fano Resonance Driven by Second Harmonic Generation, *Phys. Rev. Lett.* **118**, 063602 (2017).
- [10] E. H. El Boudouti, T. Mrabti, H. Al-Wahsh, B. DjafariRouhani, A. Akjouj, and L. Dobrzynski, Transmission gaps and Fano resonances in an acoustic waveguide: Analytical model, *J. Phys. Condens. Matter* **20**, 255212 (2008).
- [11] H. L. Zhang, Y. F. Zhu, B. Liang, J. Yang, J. Yang, and J. C. Cheng, Omnidirectional ventilated acoustic barrier, *Appl. Phys. Lett.* **111**, 203502 (2017).
- [12] Z. X. Qiang, H. J. Yang, S. Chunwongin, D. Y. Zhao, Z. Q. Ma, and W. D. Zhou, Design of Fano broadband reflectors on SOI, *IEEE Photonics Technol. Lett.* **22**, 15 (2010).
- [13] C. H. Wu, A. Khanikaev, and G. Shvets, Broadband Slow Light Metamaterial Based on a Double-Continuum Fano Resonance, *Phys. Rev. Lett.* **106**, 107403 (2011).
- [14] B. C. P. Sturmberg, K. B. Dossou, L. C. Botten, R. C. McPhedran, and C. M. de Sterke, Fano resonances of dielectric gratings: Symmetries and broadband filtering, *Opt. Express* **23**, A1672 (2015).
- [15] M. McCloskey, A. Caramazza, and B. Green, Curvilinear motion in the absence of external forces: Naive beliefs about the motion of objects, *Science* **210**, 1139 (1980).
- [16] K. A. Smith and E. Vul, Sources of uncertainty in intuitive physics, *Top. Cogn. Sci.* **5**, 185 (2013).
- [17] H. T. Zhou, W. X. Fu, Y. F. Wang, Y. S. Wang, V. Laude, and C. Zhang, Ultra-broadband passive acoustic metasurface for wide-angle carpet cloaking, *Mater. Design* **199**, 109414 (2021).
- [18] X. Lin, Y. Rivenson, N. T. Yardimci, M. Velí, Y. Luo, M. Jarrahi, and A. Ozcan, All-optical machine learning using diffractive deep neural networks, *Science* **361**, 1004 (2018).
- [19] C. Qian, B. Zheng, Y. C. Shen, L. Jing, E. P. Li, L. Shen, and H. S. Chen, Deep-learning-enabled self-adaptive microwave cloak without human intervention, *Nat. Photonics* **14**, 383 (2020).
- [20] J. Q. Jiang, M. K. Chen, and J. A. Fan, Deep neural networks for the evaluation and design of photonic devices, *Nat. Rev. Mater.* **6**, 679 (2020).
- [21] L. Xu, M. Rahmani, Y. Ma, D. A. Smirnova, K. Z. Kamali, F. Deng, Y. K. Chiang, L. Huang, H. Zhang, S. Gould, D. N. Neshev, and A. E. Miroshnichenko, Enhanced light-matter interactions in dielectric nanostructures via machine-learning approach, *Adv. Photonics* **2**, 026003 (2020).
- [22] B. Zheng, J. Yang, B. Liang, and J. C. Cheng, Inverse design of acoustic metamaterials based on machine learning using a Gauss-Bayesian model, *J. Appl. Phys.* **128**, 134902 (2020).
- [23] J. W. Jung, J. E. Kim, and J. W. Lee, Acoustic metamaterial panel for both fluid passage and broadband soundproofing in the audible frequency range, *Appl. Phys. Lett.* **112**, 041903 (2018).
- [24] C. Shen, Y. Xie, J. Li, S. A. Cummer, and Y. Jing, Acoustic metacages for sound shielding with steady air flow, *J. Appl. Phys.* **123**, 124501 (2018).
- [25] X. Wu, K. Y. Au-Yeung, X. Li, R. C. Roberts, J. Tian, C. Hu, Y. Huang, S. Wang, Z. Yang, and W. Wen, High-efficiency ventilated metamaterial absorber at low frequency, *Appl. Phys. Lett.* **112**, 103505 (2018).
- [26] Z. X. Xu, H. Gao, Y. J. Ding, J. Yang, B. Liang, and J. C. Cheng, Topology-Optimized Omnidirectional Broadband Acoustic Ventilation Barrier, *Phys. Rev. Appl.* **14**, 054016 (2020).
- [27] G. Ma, M. Yang, Z. Yang, and P. Sheng, Low-frequency narrow-band acoustic filter with large orifice, *Appl. Phys. Lett.* **103**, 011903 (2013).
- [28] Z. Chen, L. Fan, S. Y. Zhang, H. Zhang, X. J. Li, and J. Ding, An open-structure sound insulator against low-frequency and wide-band acoustic waves, *Appl. Phys. Express* **8**, 107301 (2015).
- [29] V. M. García-Chocano, S. Cabrera, and J. Sánchez-Dehesa, Broadband sound absorption by lattices of microperforated cylindrical shells, *Appl. Phys. Lett.* **101**, 184101 (2012).
- [30] L. J. Li, B. Zheng, L. M. Zhong, J. Yang, B. Liang, and J. C. Cheng, Broadband compact acoustic absorber with high-efficiency ventilation performance, *Appl. Phys. Lett.* **113**, 103501 (2018).
- [31] R. Ghaffarivardavagh, J. Nikolajczyk, S. Anderson, and X. Zhang, Ultra-open acoustic metamaterial silencer based on Fano-like interference, *Phys. Rev. B* **99**, 024302 (2019).
- [32] M. Sun, X. S. Fang, D. X. Mao, X. Wang, and Y. Li, Broadband Acoustic Ventilation Barriers, *Phys. Rev. Appl.* **13**, 044028 (2020).
- [33] S. Chen, Y. Fan, Q. Fu, H. Wu, Y. Jin, J. Zheng, and F. Zhang, A review of tunable acoustic metamaterials, *Appl. Sci.* **8**, 1480 (2018).
- [34] Z. X. Xu, M. H. Yang, A. Chen, J. Yang, B. Liang, and J. C. Cheng, Tunable low-frequency and broadband acoustic metamaterial absorber, *J. Appl. Phys.* **129**, 094502 (2021).
- [35] K. Lee, M. Jung, and S. Lee, Highly tunable acoustic metamaterials based on a resonant tubular array, *Phys. Rev. B* **86**, 184302 (2012).

- [36] B. Y. Xie, K. Tang, H. Cheng, Z. Y. Liu, S. Q. Chen, and J. G. Tian, Coding acoustic metasurfaces, *Adv. Mater.* **29**, 1603507 (2017).
- [37] O. Bilal, A. Foehr, and C. Daraio, Reprogrammable phononic metasurfaces, *Adv. Mater.* **29**, 1700628 (2017).
- [38] S. Babaei, N. Viard, P. Wang, N. Fang, and K. Bertoldi, Harnessing deformation to switch on and off the propagation of sound, *Adv. Mater.* **28**, 1631 (2016).
- [39] N. Yu, P. Genevet, M. A. Kats, F. Aieta, J.-P. Tetienne, F. Capasso, and Z. Gaburro, Light propagation with phase discontinuities: Generalized laws of reflection and refraction, *Science* **334**, 333 (2011).
- [40] Y. Xie, W. Wang, H. Chen, A. Konneker, B.-I. Popa, and S. A. Cummer, Wavefront modulation and subwavelength diffractive acoustics with an acoustic metasurface, *Nat. Commun.* **5**, 5553 (2014).
- [41] Y. Li, X. Jiang, R. Li, B. Liang, X. Zou, L. Yin, and J. Cheng, Experimental Realization of Full Control of Reflected Waves with Subwavelength Acoustic Metasurfaces, *Phys. Rev. Appl.* **2**, 064002 (2014).
- [42] X. Ni, N. K. Emani, A. V. Kildishev, A. Boltasseva, and V. M. Shalaev, Broadband light bending with plasmonic nanoantennas, *Science* **335**, 427 (2012).
- [43] F. Aieta, P. Genevet, M. A. Kats, N. Yu, R. Blanchard, Z. Gaburro, and F. Capasso, Aberration-free ultrathin flat lenses and axicons at telecom wavelengths based on plasmonic metasurfaces, *Nano Lett.* **12**, 4932 (2012).
- [44] B. A. Slovick, Z. G. Yu, and S. Krishnamurthy, Generalized effective-medium theory for metamaterials, *Phys. Rev. B* **89**, 155118 (2014).
- [45] I. Khromova, A. Sayanskiy, A. Uryutin, and A. B. Evlyukhin, Polarity of the fano resonance in the near-field magnetic-dipole response of a dielectric particle near a conductive surface, *Laser Photonics Rev.* **12**, 1800037 (2018).
- [46] See Supplemental Material at <http://link.aps.org/supplemental/10.1103/PhysRevApplied.16.044020> for the Gauss-Bayesian model for training and prediction, the effective refractive index and mass density ratios in the double-helix metastructure, transmission spectra under oblique incidence, and simulated transmission spectra with and without viscothermal loss.
- [47] B. Shahriari, K. Swersky, Z. Wang, R. P. Adams, and N. de Freitas, Taking the human Out of the loop: A review of Bayesian optimization, *Proc. IEEE* **104**, 148 (2016).
- [48] J. Snoek, H. Larochelle, and R. Adams, Practical Bayesian optimization of machine learning algorithms, *Adv. Neural. Inf. Process. Syst.* **25**, 2960 (2012).
- [49] X. F. Zhu, K. Li, P. Zhang, J. Zhu, J. T. Zhang, C. Tian, and S. C. Liu, Implementation of dispersion-free slow acoustic wave propagation and phase engineering with helical-structured metamaterials, *Nat. Commun.* **7**, 11731 (2016).
- [50] V. Fokin, M. Ambati, C. Sun, and X. Zhang, Method for retrieving effective properties of locally resonant acoustic metamaterials, *Phys. Rev. B* **76**, 144302 (2007).
- [51] M. Yang, G. C. Ma, Z. Y. Yang, and P. Sheng, Coupled Membranes with Doubly Negative Mass Density and Bulk Modulus, *Phys. Rev. Lett.* **110**, 134301 (2013).
- [52] Y. S. Choy and L. X. Huang, Experimental studies of a drumlike silencer, *J. Acoust. Soc. Am.* **112**, 2026 (2002).